Computers and Mathematics with Applications 176 (2024) 67–76

Contents lists available at ScienceDirect

Computers and Mathematics with Applications

journal homepage: www.elsevier.com/locate/camwa

A novel phase-field model for three-dimensional shape transformation

Seokjun Ham [a], Hyundong Kim [b,c], Youngjin Hwang [a], Soobin Kwak [a], Jyoti [d], Jian Wang [e], Heming Xu [e], Wenjing Jiang [e], Junseok Kim [a,*]

[a] Department of Mathematics, Korea University, Seoul 02841, Republic of Korea
[b] Department of Mathematics and Physics, Gangneung-Wonju National University, Gangneung 25457, Republic of Korea
[c] Institute for Smart Infrastructure, Gangneung-Wonju National University, Gangneung 25457, Republic of Korea
[d] The Institute of Basic Science, Korea University, Seoul 02841, Republic of Korea
[e] School of Mathematics and Statistics, Nanjing University of Information Science and Technology, Nanjing, 210044, China

ARTICLE INFO

Keywords:
Robust numerical method
Shape transformation
Phase-field model
Modified Allen–Cahn equation

ABSTRACT

We present a simple and robust numerical technique for a novel phase-field model of three-dimensional (3D) shape transformation. Shape transformation has been achieved using phase-field models. However, previous phase-field models have intrinsic drawbacks, such as shrinkage due to motion by mean curvature and unwanted growth. To overcome these drawbacks associated with previous models, we propose a novel phase-field model that eliminates these shortcomings. The proposed phase-field model is based on the Allen–Cahn (AC) equation with nonstandard mobility and a nonlinear source term. To numerically and efficiently solve the proposed phase-field equation, we adopt an operator splitting method, which consists of the AC equation with a nonstandard mobility and a fidelity equation. The modified AC equation is solved using a fully explicit finite difference method with a time step that ensures stability. For solving the fidelity equation, we use a semi-implicit scheme with a frozen coefficient. We have performed several numerical experiments with various 3D sources and target shapes to verify the robustness and efficacy of our proposed mathematical model and its numerical method.

1. Introduction

Shape transformation is the process of changing the shape of an object. In the context of computer graphics and image processing, shape transformation typically involves manipulating the geometric properties of an object to achieve a desired shape. There are several types of shape transformations. In this study, we focus on morphing, which is a technique used to smoothly transform one shape into another by creating a sequence of intermediate shapes. Shape transformation has been widely used in animation [1,2], computer vision [3,4], volume reconstruction [5], and metal casting [6]. Various studies have been conducted on shape transformation in two dimensions (2D) as well as in three dimensions (3D) [5,7]. One notable study was performed by Alexander et al. who developed a new method for deforming two arbitrary topological 2D shapes with complex textures. Their method combined space-time transfinite interpolation, generating smooth transitions between the source and target shapes without requiring any correspondence between boundary points or features. Weng et al. [1] explored a 2D shape deformation method based on nonlinear least squares optimization, which effectively preserves the two local shape characteristics. In order to preserve as much local detail as possible in surface deformation operations, Qin et al. [8] developed a method for controlling the stiffness of a surface by changing the size of local elements. The overall stiffness of the shape is determined by the size of the local element.

Meanwhile, with the development of 3D technology, research on the shape transformation of 3D objects has become increasingly important. Machine learning has enabled the development of new, more efficient, and accurate methods for shape transformation. For example, Gao et al. [9] developed a novel mesh deformation automatic transfer architecture that can be used to transform shapes even if they do not match. In addition, the phase-field model, based on the Allen–Cahn (AC) equation [10], has been shown to be very effective in shape transformation [7,11–15]. The AC equation, proposed by Allen and Cahn in 1979, satisfies the maximum principle and holds the property that the total energy of the system decreases over time [10]. The AC equation has been applied in many fields, such as materials science [16,17], image seg-

* Corresponding author.
E-mail address: cfdkim@korea.ac.kr (J. Kim).
URL: https://mathematicians.korea.ac.kr/cfdkim (J. Kim).

https://doi.org/10.1016/j.camwa.2024.09.006
Received 24 January 2024; Received in revised form 8 August 2024; Accepted 11 September 2024
Available online 18 September 2024

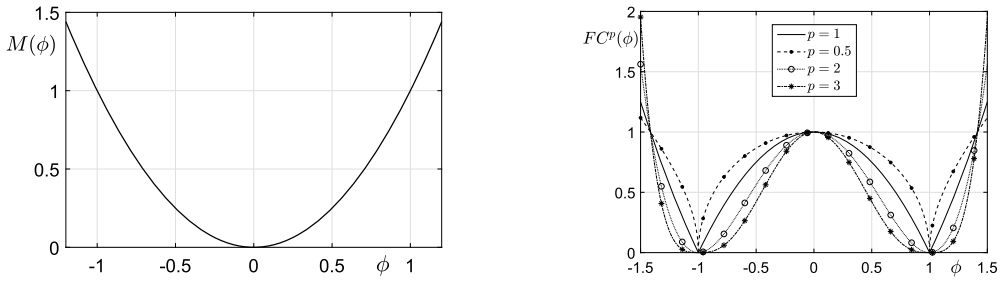

Fig. 1. (a) Non-standard variable mobility $M(\phi) = \phi^2$. (b) $FC^p(\phi)$ for $p = 0.5$, 1, 2, and 3.

mentation [18–21], data assimilation [22], topology optimization [23], and reconstruction [24]. Wang and Shi [24] proposed a new surface reconstruction method based on the modified AC equation. Research on the conservative AC (CAC) equation, which is one of the modified forms of the AC equation and conserves mass, has been actively conducted in studies [25–27]. A high-order energy stable scheme for the CAC equation was presented in [25]. Cui et al. [26] proposed an operator splitting scheme for solving the nonlocal CAC equation. Sun and Zhang [27] presented a radial basis function method for solving the CAC equation on smooth compact surfaces embedded in 3D. Kim et al. [5] improved the AC equation and applied it to the 3D volume reconstruction of multi-slice data. Li et al. [28] efficiently performed volume inpainting using the modified AC equation. Furthermore, in shape transformation, many researchers have used the AC equation. For example, Wang et al. [14] proposed a 3D shape transformation method based on the phase-field model, including a modified AC equation. This method can handle shape transformations of objects with sharp boundaries and different topologies.

Shape transformation is used in a variety of applications, including metal casting [11,29], which requires sensible rearrangement of shapes. During the process of metal casting, the source shape undergoes various undesirable localized deformations to produce the desired shape. Traditionally, time-consuming and costly experiments are performed to identify material properties through trial and error routines. However, computational experiments using mathematical modeling and numerical methods provide a more efficient way to save both cost and time. In the literature, numerous research studies [7,11,30] have been conducted on the casting process. For example, Si et al. [31] used the finite difference method for heat flow and the finite element method for thermo-elasto-plastic stress analysis during the casting process. To calculate the heat flux and heat transfer coefficient at the interface of the metal-sand mold, an inverse conduction model was used in [32]. Furthermore, Fieres et al. [29] used computed tomography and an immersed boundary finite element method to simulate pore-scale defects in the casting and molding process. Additionally, to predict the location of shrinkage defects like porosity and cracks, auto cast software for contact wheel was used by [33].

More recently, Kim et al. [11] discussed an example of metal casting by using a phase-field model to improve the quality of the product in the mechanical field. Their method efficiently deals with the time step constraint during the solution of the diffusion term. However, for more complex 3D shapes, the model shows discontinuity in the shape transformation process due to motion by mean curvature. In this paper, we address these problems by proposing a modified phase-field model with nonstandard mobility, fidelity, and a nonlinear source term. The governing model is solved numerically using an operator splitting method. The diffusion term is solved using a fully explicit finite difference method, and the fidelity term is solved using a semi-implicit scheme. Nonstandard mobility in the diffusion term and a frozen coefficient in the fidelity term are used to improve the accuracy and stability of the numerical solution. The method is validated with several numerical experiments on 3D sources and targets. The computational results show that the model can accurately and realistically simulate changes in the shape of a material, which can be applied in the casting of metals.

This paper is organized as follows. In Section 2, the proposed equation and its numerical method are presented. Section 3 presents comparison tests and various experiments on shape transformation. Conclusions are given in Section 4.

2. Modified AC equation and its numerical method

2.1. Governing equation

We propose the following new modified Allen–Cahn (AC) equation with a fidelity term for modeling shape transformation:

$$\frac{\partial \phi(\mathbf{x},t)}{\partial t} = M(\phi(\mathbf{x},t))\left(-\frac{F'(\phi(\mathbf{x},t))}{\epsilon^2} + \Delta\phi(\mathbf{x},t)\right) + \alpha FC^p(\phi(\mathbf{x},t))(\psi(\mathbf{x}) - \phi(\mathbf{x},t)), \tag{1}$$

where $F(\phi) = 0.25(\phi^2 - 1)^2$ is a double-well potential, $\phi(\mathbf{x},t)$ is the phase-field, and $\psi(\mathbf{x})$ is a target shape. Here, $M(\phi(\mathbf{x},t)) = \phi^2(\mathbf{x},t)$ is a non-standard variable mobility, ϵ is an interfacial transition parameter, $FC(\phi) = |\phi^2 - 1|$ is fidelity coefficient, α is a fidelity parameter, p is a positive parameter. We note that if $M(\phi(\mathbf{x},t)) = 1$ and $\alpha = 0$, then Eq. (1) becomes the conventional AC equation [10,34], i.e.,

$$\frac{\partial \phi(\mathbf{x},t)}{\partial t} = -\frac{F'(\phi(\mathbf{x},t))}{\epsilon^2} + \Delta\phi(\mathbf{x},t). \tag{2}$$

The non-standard variable mobility $M(\phi)$ and $FC^p(\phi)$ are illustrated in Figs. 1(a) and (b), respectively. The non-standard variable mobility, denoted as $M(\phi)$, prevents the motion by mean curvature, while the term $\alpha FC^p(\phi)$ restricts growth to the non-interfaces. To examine the effect of non-standard mobility, let us consider the following equation with $\alpha = 0$ from Eq. (2):

$$\frac{\partial \phi(\mathbf{x},t)}{\partial t} = M(\phi(\mathbf{x},t))\left(-\frac{F'(\phi(\mathbf{x},t))}{\epsilon^2} + \Delta\phi(\mathbf{x},t)\right). \tag{3}$$

Figs. 2(a) and (b) illustrate the temporal evolutions for the classical AC equation (2) and the AC equation with non-standard mobility (3), respectively, at the same time. In the case of the classical AC equation, the interface exhibits shrinkage due to the effect of motion by mean curvature. Conversely, when non-standard mobility is introduced, the mobility is zero at the interface ($\phi = 0$), which prevents the interface from shrinking and allows it to maintain its shape. To provide a visual representation, Fig. 3 illustrates schematic for the dynamics of the proposed model in two-dimensional space. Figs. 3(a)–(c) represent the temporal evolution of the zero-level contour of ϕ, ϕ with its zero-level set, and the fidelity term in Eq. (2), $\alpha FC^p\phi(\psi - \phi)$, respectively. From the results shown in Fig. 3(c), for the interface of ϕ, the fidelity term is positive on the side that is adjacent to the target ψ and negative on the side that is not. Consequently, the fidelity term drives ϕ to conform to the target shape.

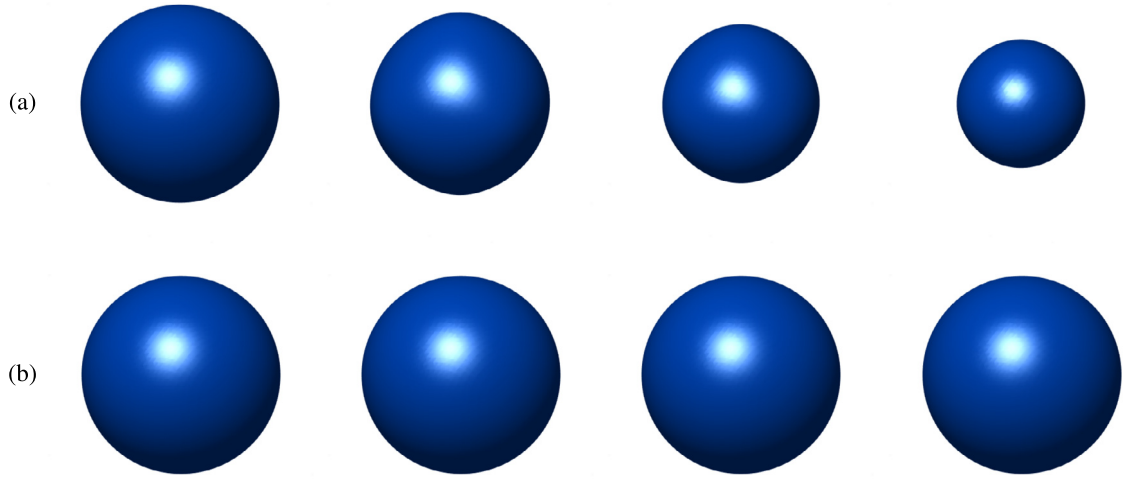

Fig. 2. Dynamics over time for the (a) classical AC equation (2) and (b) AC equation with non-standard mobility (3).

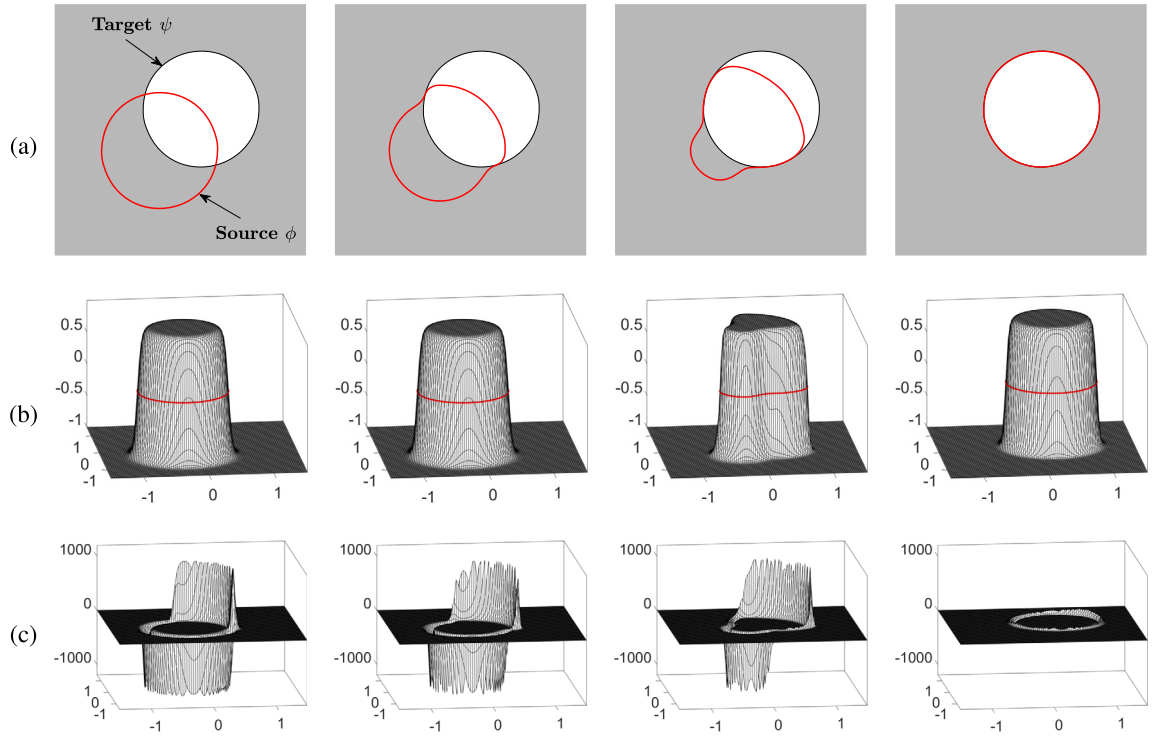

Fig. 3. Schematic illustration for the dynamics of the proposed model in two-dimensional space. (a) Temporal evolution of the zero-level contour of ϕ with target. (b) Temporal evolution of ϕ with its zero-level set. (c) Temporal evolution of the fidelity term in Eq. (2), $\alpha FC^p\phi(\psi-\phi)$.

2.2. Computational algorithm

We discretize $\Omega=(x_l,x_r)\times(y_l,y_r)\times(z_l,z_r)$ as $\Omega_h=\{(x_i,y_j,z_k)=(x_l+(i-0.5)h,y_l+(j-0.5)h,z_l+(k-0.5)h)\}$, where $1\le i\le N_x$, $1\le j\le N_y$, and $1\le k\le N_z$ with a uniform grid size h. Moreover, we use the notations ϕ^n_{ijk} and ψ_{ijk} to represent $\phi(x_i,y_j,z_k,n\Delta t)$ and $\psi(x_i,y_j,z_k)$, respectively, where Δt is the time step size. By employing the operator splitting method, we can decompose Eq. (1) into the following separate equations:

$$\frac{\partial\phi(\mathbf{x},t)}{\partial t}=M(\phi(\mathbf{x},t))\left(-\frac{F'(\phi(\mathbf{x},t))}{\epsilon^2}+\Delta\phi(\mathbf{x},t)\right), \tag{4}$$

$$\frac{\partial\phi(\mathbf{x},t)}{\partial t}=\alpha FC^p(\phi(\mathbf{x},t))(\psi(\mathbf{x})-\phi(\mathbf{x},t)). \tag{5}$$

To obtain the numerical solution of the governing Eq. (1), we can follow a two-step process. Firstly, we employ the explicit Euler method to solve the AC equation (4)

$$\frac{\phi^*_{ijk}-\phi^n_{ijk}}{\Delta t}=M(\phi^n_{ijk})\left(-\frac{F'(\phi^n_{ijk})}{\epsilon^2}+\Delta_d\phi^n_{ijk}\right), \tag{6}$$

where $\Delta_d\phi^n_{ijk}=(\phi^n_{i+1,jk}+\phi^n_{i-1,jk}+\phi^n_{i,j+1,k}+\phi^n_{i,j-1,k}+\phi^n_{ij,k+1}+\phi^n_{ij,k-1}-6\phi^n_{ijk})/h^2$. From Eq. (6), we can obtain the intermediate solution ϕ^*_{ijk} as follows:

$$\phi^*_{ijk}=\phi^n_{ijk}+\Delta tM(\phi^n_{ijk})\left(-\frac{F'(\phi^n_{ijk})}{\epsilon^2}+\Delta_d\phi^n_{ijk}\right). \tag{7}$$

Next, the fidelity term is solved using the semi-implicit scheme with a frozen coefficient using Eq. (5).

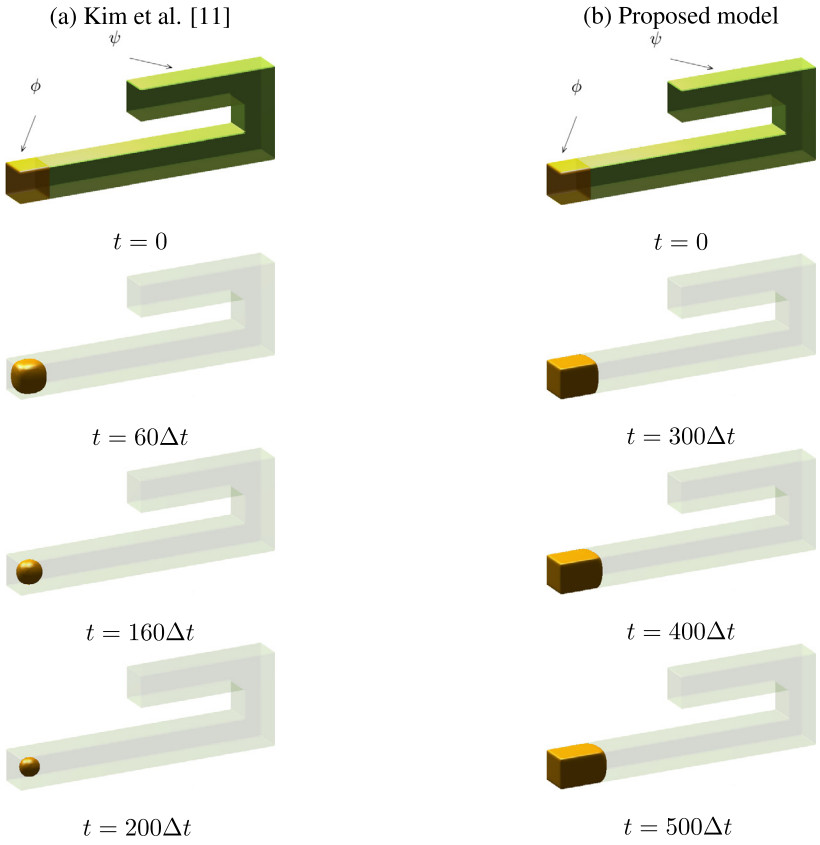

Fig. 4. Temporal evolutions to numerical solutions of the model in (a) Kim et al. [11] (left) and (b) proposed model (right) with $\alpha = 100$.

$$\frac{\phi_{ijk}^{n+1} - \phi_{ijk}^{*}}{\Delta t} = \alpha F C^{p}\left(\phi_{ijk}^{*}\right)(\psi_{ijk} - \phi_{ijk}^{n+1}). \tag{8}$$

Eq. (8) can be rewritten as

$$\phi_{ijk}^{n+1} = \frac{\phi_{ijk}^{*} + \Delta t \alpha \psi_{ijk} F C^{p}\left(\phi_{ijk}^{*}\right)}{1 + \Delta t \alpha F C^{p}\left(\phi_{ijk}^{*}\right)}. \tag{9}$$

One time step iteration is calculated by this process.

2.3. Stability analysis

In this section, we present the stability analysis of the proposed numerical method and propose a time step constraint, which guarantees the discrete maximum principle for the numerical solution of the proposed model. We suppose that the time step Δt, initial condition, and target satisfy the following conditions:

$$\Delta t \le \frac{\epsilon^2 h^2}{2h^2 + 6\epsilon^2},\ |\phi_{ijk}^{0}| \le 1,\ \text{and}\ |\psi_{ijk}| \le 1, \tag{10}$$

for $1 \le i \le N_x$, $1 \le j \le N_y$, and $1 \le k \le N_z$.

Initially, we consider the first step in the AC Eq. (7) with the mobility. Since, we set the non-standard variable mobility as $M(\phi) = \phi^2$, $0 \le M(\phi) \le 1$ for $|\phi| \le 1$. Therefore, by the theorem in [35], the intermediate solution is bounded as

$$|\phi_{ijk}^{*}| \le 1, \quad \text{for} \quad 1 \le i \le N_x, 1 \le j \le N_y, \text{ and } 1 \le k \le N_z, \tag{11}$$

if the time step satisfies

$$\Delta t \le \frac{\epsilon^2 h^2}{2h^2 + 6\epsilon^2}. \tag{12}$$

Then, we examine the next step in Eq. (8) using the semi-implicit scheme. From Eq. (9),

$$|\phi_{ijk}^{n+1}| \le 1, \quad \text{for} \quad 1 \le i \le N_x, 1 \le j \le N_y, \text{ and } 1 \le k \le N_z, \tag{13}$$

for any time step Δt, provided $|\phi_{ijk}^{*}| \le 1$ and $|\psi_{ijk}| \le 1$. Therefore, the proposed numerical method for shape transformation is stable and satisfies the discrete maximum principle, under the following time step constraint.

$$\Delta t \le \frac{\epsilon^2 h^2}{2h^2 + 6\epsilon^2}. \tag{14}$$

3. Computational tests

A numerical equilibrium state is determined by the discrete l_2-norm of the difference between two consecutive solutions, which must be smaller than a specified tolerance, tol. That is,

$$||\phi^{n} - \phi^{n-1}||_2 = \sqrt{\sum_{i=1}^{N_x}\sum_{j=1}^{N_y}\sum_{k=1}^{N_z}\left(\phi_{ijk}^{n} - \phi_{ijk}^{n-1}\right)^2 \Big/ (N_x N_y N_z)} < tol,$$

where we set $tol = 1.0e\text{-}6$ for the following numerical experiments, unless otherwise specified.

3.1. Comparison test with a previous model

In this section, we compare the previous and proposed models. First, we introduce the previous model. The previous shape transformation model was proposed by Kim et al. [11] as follows:

$$\frac{\partial \phi}{\partial t} = -\frac{F'(\phi)}{\epsilon^2} + \Delta\phi + \alpha\sqrt{F(\phi)}(\psi - \phi), \tag{15}$$

where ϕ is a source and ψ is a target. For the source shape, we chose a cube and for the target shape, we chose a U-shaped bar to perform some comparison tests as shown in the first row of Fig. 4. For the proposed model, we use the non-standard variable mobility $M(\phi) = \phi^2$ and

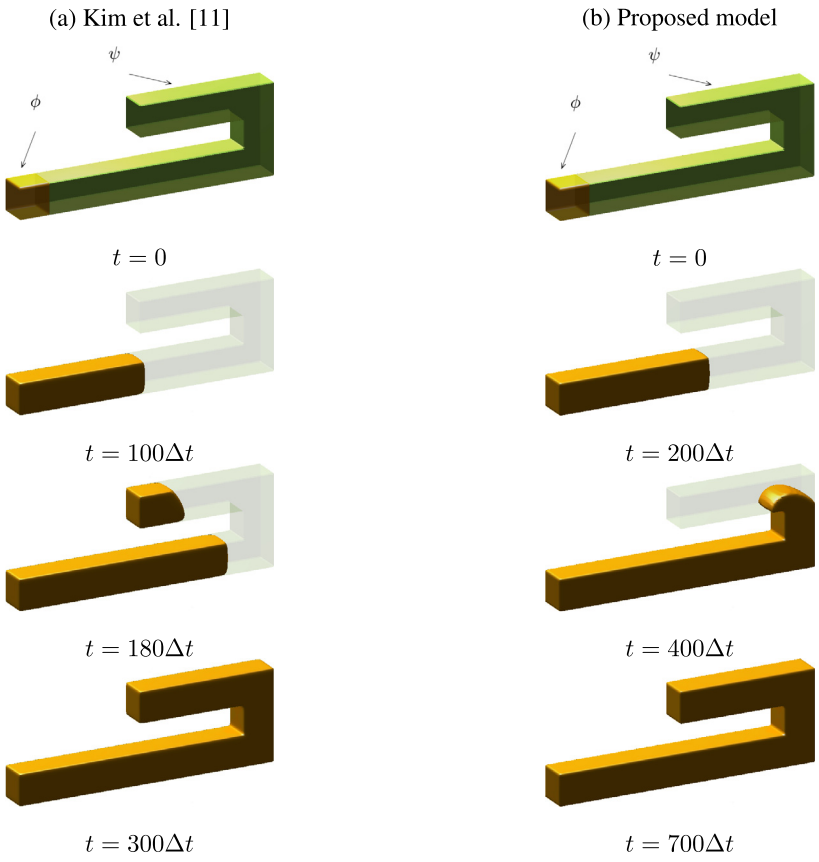

Fig. 5. Temporal evolutions to numerical solutions of the model in (a) Kim et al. [11] (left) and (b) proposed model (right) with $\alpha = 10000$.

$FC^2(\phi) = |\phi^2 - 1|^2$ in a three-dimensional space $\Omega = (-2, 2) \times (-1, 1) \times (-1, 1)$. We use the uniform grid $h = 1/50$, time step $\Delta t = 0.12h^2$, and $\epsilon = 5h$. We note that the time step $\Delta t = 0.12h^2$ satisfies the time step constraint (14) for the stability. We compare the dynamics of two different models with $\alpha = 100$ and $\alpha = 10000$. Figs. 4(a) and (b) show the temporal evolutions of the model in [11] and the proposed model, respectively, with $\alpha = 100$. For the case of [11], the numerical solution significantly shrinks due to the mean curvature effect. On the other hand, in the case of the proposed model, the mean curvature effect is substantially reduced owing to the non-standard variable mobility. Fig. 5 has two columns, which show the snapshots of the previous and proposed models with $\alpha = 10000$. In the previous model, the phenomenon of growth occurred at non-interfaces. While it was greatly reduced by the effect of $FC^2(\phi)$ in the proposed model. In the novel proposed model, the mean curvature flow phenomenon for small α and non-consistent growth phenomenon at non-interfaces for large α were greatly reduced.

Next, we consider the efficiency of the proposed method. The parameters used are $\Delta t = 0.1h^2$, $\epsilon = h$, and $tol = 1.0e\text{-}5$. As the fidelity parameter α increases, the growth rate becomes faster in both the previous and proposed methods. In the previous method, there is growth occurs at non-interfaces when the value of α is large. Therefore, we compare the previous model, using α values with and without growth at non-interfaces, with the proposed model using a large α. In the previous model, we use the fidelity parameter $\alpha = 3800$ where growth occurs at non-interfaces and $\alpha = 3600$ where growth does not occur at non-interfaces. In the proposed model, we use $\alpha = 20000$. The other parameters and initial conditions are the same as those used in the numerical experiments above.

Fig. 6 shows the temporal evolution of numerical solutions for the previous and proposed models. In Figs. 6(a) and (b), we use the previous models with $\alpha = 3800$ and $\alpha = 3600$, respectively, and in Fig. 6(c), we use the proposed model with $\alpha = 20000$. We observed that the growth at non-interfaces when $\alpha = 3800$, and the total number of iterations required to reach the numerical equilibrium state using the previous model is greater than the total number of iterations using the proposed model. Furthermore, we observed that the numerical solution using the proposed model grows more accurately to the target shape than the numerical solution using the previous model. We define the total number of iterations required to reach the equilibrium state as N_t. Table 1 lists the CPU times and the total number of iterations required to reach the equilibrium state using the previous and proposed models. We observed that the CPU time and N_t using the proposed model are both less than those using the previous model.

3.2. Effect of parameters

In this section, we investigate the parameters α, p, and ϵ in the proposed model (1). For the numerical tests, we consider two cubes in three-dimensional computational domain $\Omega = (-1, 1) \times (-1, 1) \times (-1, 1)$, with one designated as the source and the other as the target. The source and target cubes are illustrated in the first column of Fig. 7. Here, the parameters for discretization in space and time are $N_x = N_y = N_z = 100$, $h = 1/50$, and $\Delta t = 0.12h^2$.

First, we investigate the effect of the parameter α in the fidelity term. Fig. 7 shows the temporal evolutions of numerical results for $\alpha = 10^4$, $\alpha = 10^5$, and $\alpha = 10^6$. Here, we fix the other parameters as $\epsilon = 5h$ and $p = 2$. From the results shown in Fig. 7, as α increases, we can observe that the rate of shape evolution accelerates. However, when α becomes excessively large, the interface of the shape becomes irregular and jagged. Therefore, an appropriate value for α should be chosen based on the considerations of evolution speed and efficiency.

Next, we investigate the effect of the parameter p in the fidelity term. Fig. 8 shows the temporal evolutions of numerical results for $p = 2$, $p = 5$, and $p = 10$. Here, we fix the other parameters as $\epsilon = 5h$ and

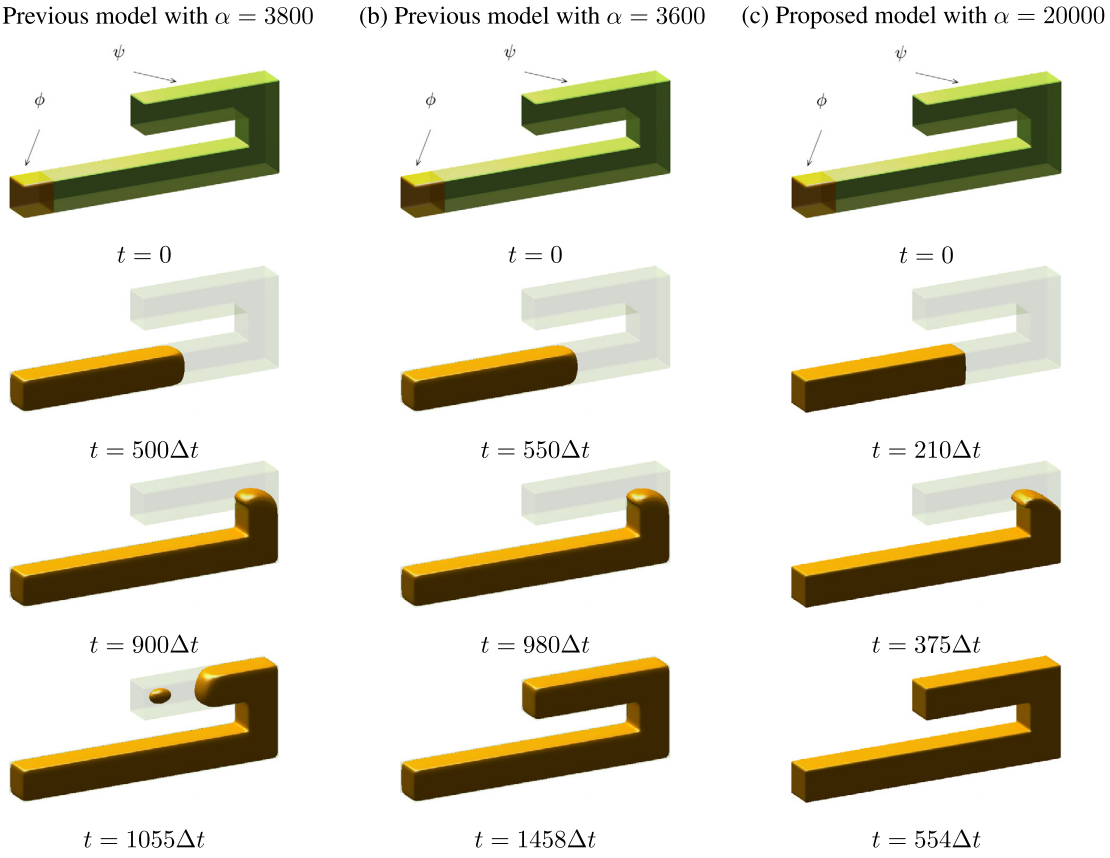

Fig. 6. Temporal evolutions to numerical solutions of the model in (a) previous model with $\alpha = 3800$, (b) previous model with $\alpha = 3600$, and (c) proposed model with $\alpha = 20000$.

Table 1
CPU times and the total number of iterations that reach the equilibrium state using the previous and proposed models.

Case	Previous model ($\alpha = 3800$)	Previous model ($\alpha = 3600$)	Proposed model ($\alpha = 20000$)
N_t	1157	1458	554
CPU time(s)	95.4186	121.3859	39.4573

$\alpha = 10^5$. As the parameter p increases, it increasingly inhibits shape transformation on the non-interfaces ($\phi \neq 0$). However, as evidenced by the results in Fig. 8, larger values of p lead to a slower rate of shape evolution, and when p becomes excessively large, the interface of the shape becomes irregular and distorted.

Finally, to investigate the effect of the parameter ϵ, we consider cubic source and u-shaped target as shown in the first column of Fig. 9. Since the parameter ϵ affects the time step constraint, we take the time step $\Delta t = 5 \times 10^{-6}$ to ensure the stability of the numerical solutions. This time step satisfies the constraint in Eq. (14) for $\epsilon = 5h$, $\epsilon = 10h$, and $\epsilon = 20h$. Here, we fix the other parameters as $\alpha = 10^5$ and $p = 2$. Fig. 9 shows the temporal evolutions of shape transformation for $\epsilon = 5h$, $\epsilon = 10h$, and $\epsilon = 20h$. In the phase-field model, the parameter ϵ influences the interface transition length. Consequently, if epsilon becomes excessively large, the interface transition length surpasses the spacing of the target shape, resulting in growth occurring in the non-interface region.

3.3. Computational experiments with various source and target shapes

3.3.1. Oval to bunny

For the simple case of shape transformation within $\Omega = (-1, 1) \times (-1, 1) \times (-1, 1)$, we chose a three-dimensional ellipsoid as the source shape and the Stanford bunny as the target shape (refer to Fig. 10(a)). The equation for the ellipsoidal shape, centered at $(-0.55, -0.58, 0.2)$, is defined as follows:

$$\phi(x, y, z, 0) = \tanh\left(\frac{1 - \sqrt{(\frac{x+0.55}{0.28})^2 + (\frac{y+0.58}{0.16})^2 + (\frac{z-0.2}{0.18})^2}}{\sqrt{2}\epsilon}\right),$$

where the semi-axes lengths in the x-, y-, and z-directions are 0.28, 0.16, and 0.18, respectively. To facilitate the transformation of three-dimensional shapes, we assign the following parameter values: $N_x = N_y = N_z = 200$, $h = 1/N_x$, $\epsilon = 5h$, $\Delta t = 0.12h^2$, and $\alpha = 100000$. From this experiment, we found that as the time increases from $t = 5\Delta t$ to $t = 175\Delta t$, the source shape starts to transform into the target shape. Within a very small number of time steps, the target shape acquired the source shape, as depicted in Figs. 10(b)–(h). Here we choose the value of fidelity parameter to be very high, $\alpha = 100000$, which allows source shape to transform into the target shape more accurately without growing in non-interfaces. Additionally, the total number of iterations required to reach the equilibrium state is very low.

3.3.2. Cuboid to complex 3D shape

Similarly for a more complex scenario, we utilize a three-dimensional cuboid as the source shape and a complex 3D shape as the target shape (refer to Fig. 11(a)) within $\Omega = (-1.1, 1.1) \times (-1.1, 1.1) \times (-1.1, 1.1)$. To

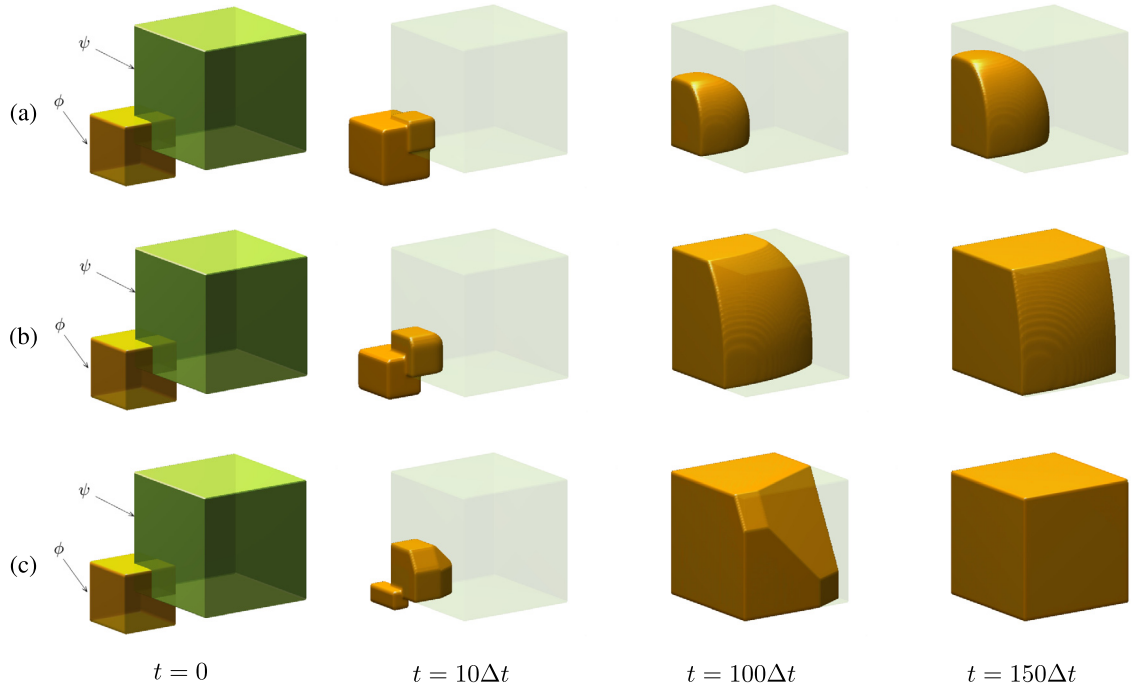

Fig. 7. Temporal evolutions of numerical results for (a) $\alpha = 10^4$, (b) $\alpha = 10^5$, and (c) $\alpha = 10^6$.

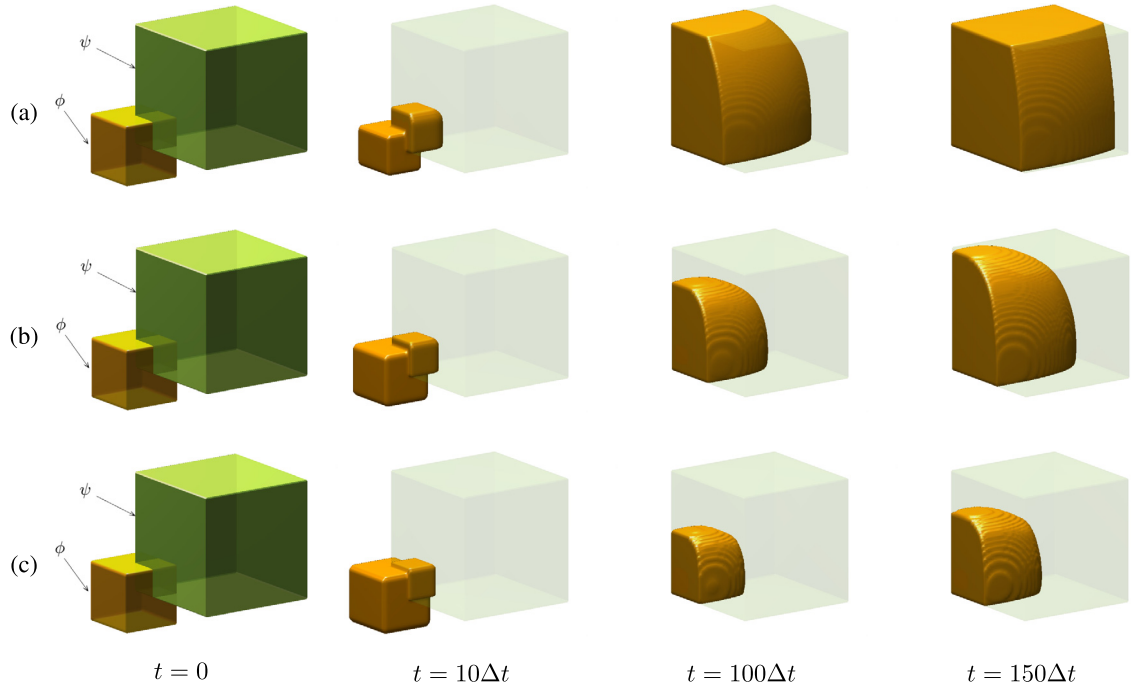

Fig. 8. Temporal evolutions of numerical results for (a) $p = 2$, (b) $p = 5$, and (c) $p = 10$.

facilitate the transformation of these three-dimensional shapes, we set the following parameters: $N_x = N_y = N_z = 44$, $h = 1/N_x$, $\epsilon = 1.5h$, $\Delta t = 0.12h^2$, and $\alpha = 3500$.

Here, we used a relatively small value for the fidelity parameter, $\alpha = 3500$, and observed that the source shape starts transforming into the complex target shape without any intermediate growth at non-interfaces. Over a brief series of time steps, from $t = 30\Delta t$ to $t = 345\Delta t$, the source shape gradually evolves into the target shape with high accuracy. Consequently, the proposed model significantly reduces the number of iterations needed to reach equilibrium, and within a short time interval, the target shape closely aligns with the source shape, as illustrated in Figs. 11(b)–(h).

3.3.3. Spheroid to 2-torus

To perform shape transformation for different topological structures in $\Omega = (-1, 1) \times (-1.5, 1.5) \times (0, 1)$, we set the source shape $\phi(x, y, z, 0)$ as a spheroid and the target shape $\psi(x, y, z)$ as a 2-torus:

$$\phi(x, y, z, 0) = \tanh\left(\frac{0.15 - \sqrt{0.2\left((x + 0.25)^2 + (y - 0.8)^2\right) + (z - 0.5)^2}}{\sqrt{2}\epsilon}\right),$$

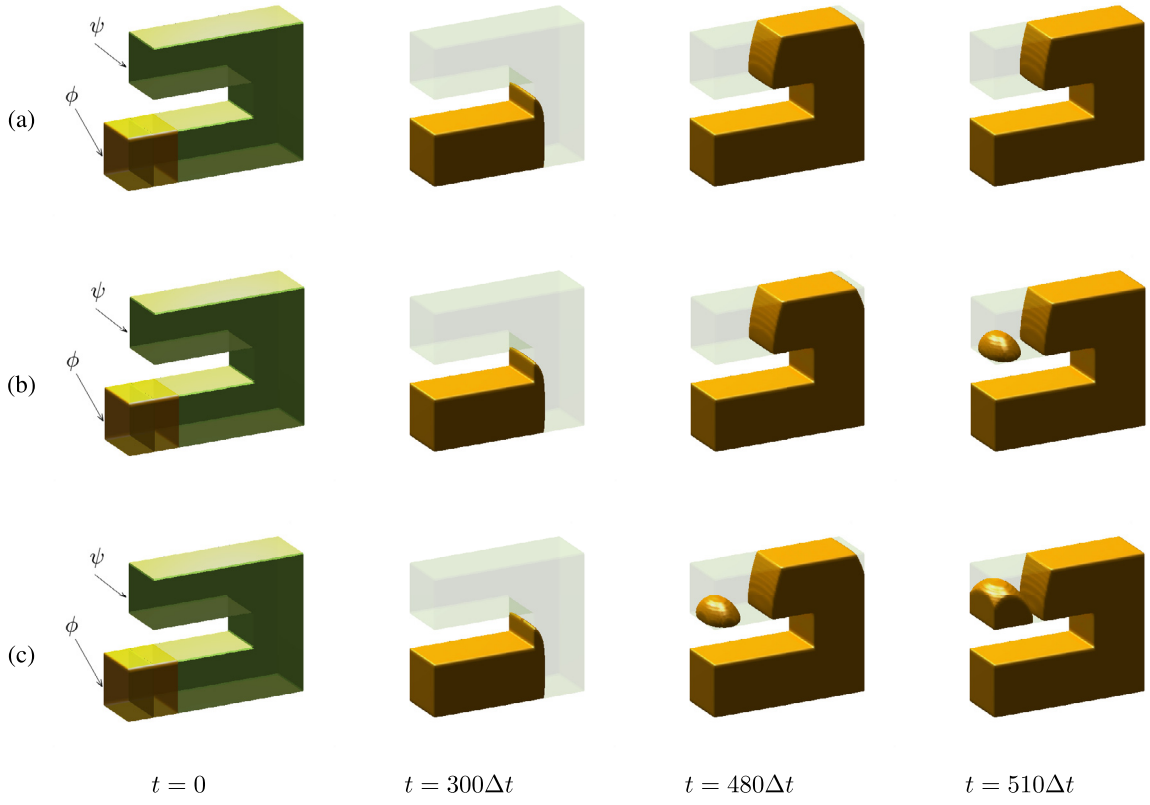

Fig. 9. Temporal evolutions of numerical results for (a) $\epsilon = 5h$, (b) $\epsilon = 10h$, and (c) $\epsilon = 20h$.

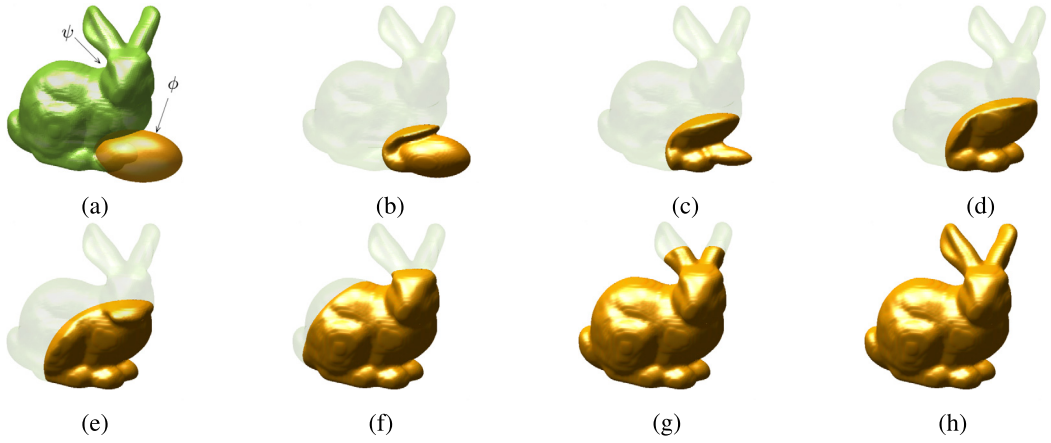

Fig. 10. (a) Initial models for oval as source $\phi(x, y, z, 0)$ and bunny as target $\psi(x, y, z)$. (b)–(h) are the snapshots of $\phi(x, y, z, t)$ at $t = 5\Delta t$, $20\Delta t$, $40\Delta t$, $60\Delta t$, $100\Delta t$, $130\Delta t$, and $175\Delta t$, respectively.

$$\psi(x, y, z) = \tanh\left(\frac{0.15 - \sqrt{d^2(x, y, z) + (z - 0.5)^2}}{\sqrt{2}\epsilon}\right),$$

where $d(x, y, z) = \left((x - 0.075)^2 + (y - 0.1)^2\right)^2 + (x - 0.25)^2 - (y - 0.15)^2$. In this test, we use the following parameter values: $N_x = 100$, $N_y = 200$, $N_z = 50$, $h = 1/50$, $\Delta t = 0.1h^2$, $\epsilon = 2h$, and $\alpha = 5000000$. With a high fidelity parameter value of $\alpha = 5000000$, the initial source spheroid $\phi(x, y, z, 0)$ transitions smoothly into the 2-torus target shape $\psi(x, y, z)$, as shown in Fig. 12(b)–(h). This transformation occurs within a few time steps, ranging from $t = \Delta t$ to $t = 120\Delta t$. As illustrated in Fig. 12, the use of non-standard variable mobility significantly reduces the mean curvature effect, enabling the target shape to closely match the source shape in a very short time interval without any intermediate growth at non-interfaces.

4. Conclusions

In this study, we have presented a robust numerical algorithm for a novel phase-field model that enables efficient and accurate 3D shape transformation. Previous phase-field models suffered from drawbacks such as shrinkage and unwanted growth, which we have successfully addressed in our proposed mathematical model. Our approach is based on the AC equation with nonstandard mobility and a nonlinear source term. By incorporating these modifications, we effectively reduced the effects of mean curvature and localized growth near the interface, resulting in improved and robust shape transformations. Numerical experiments

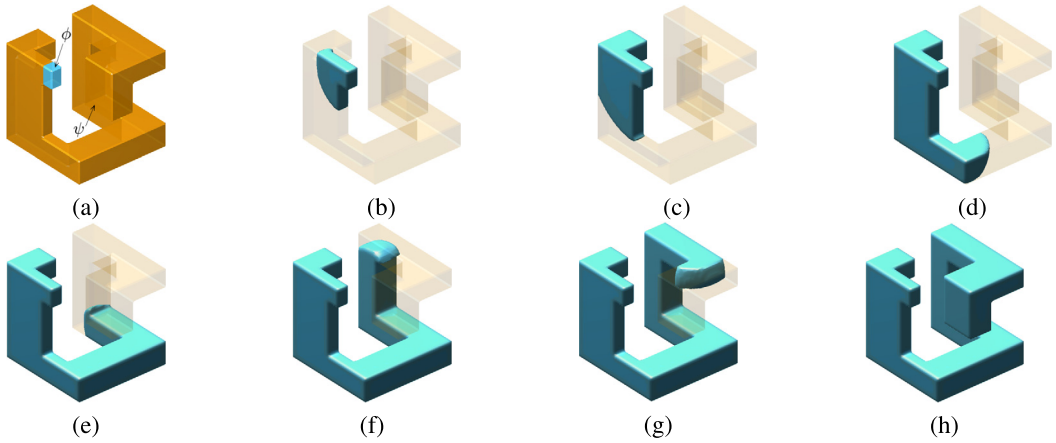

Fig. 11. (a) Initial models for cuboid as source $\phi(x, y, z, 0)$ and complex 3D as target $\psi(x, y, z)$. (b)–(h) are snapshots of $\phi(x, y, z, t)$ at $t = 30\Delta t$, $60\Delta t$, $110\Delta t$, $195\Delta t$, $250\Delta t$, $300\Delta t$ and $345\Delta t$, respectively.

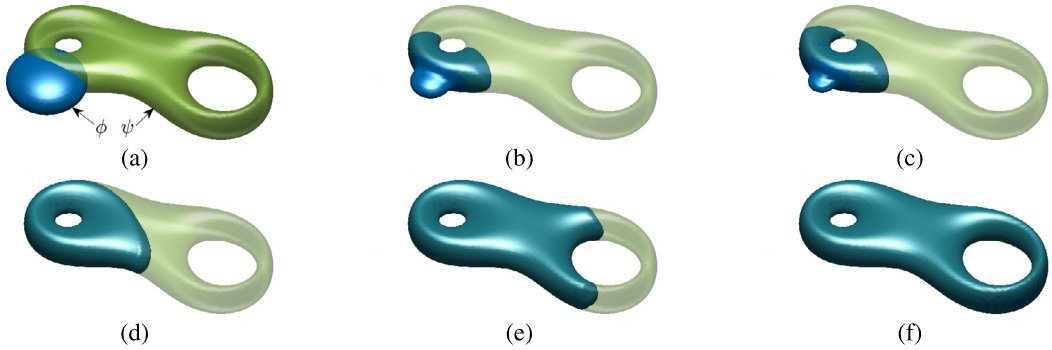

Fig. 12. (a) Initial model for spheroid as source $\phi(x, y, z, 0)$ and 2-torus as target $\psi(x, y, z)$. (b)–(f) are snapshots of $\phi(x, y, z, t)$ at $t = \Delta t$, $2\Delta t$, $20\Delta t$, $60\Delta t$, and $120\Delta t$, respectively.

with various 3D sources and target shapes demonstrate the robustness and efficacy of our proposed mathematical model and numerical solution algorithm. The computational results validate our approach to achieving smooth and accurate 3D shape transformations, overcoming the limitations of previous models. In conclusion, our work offers a simple and reliable solution for 3D shape transformation using the phase-field approach. The proposed mathematical model and numerical method have promising applications in fields requiring precise and efficient 3D shape transformations.

Data availability

Data will be made available on request.

Declaration of generative AI and AI-assisted technologies in the writing process

This article was not created using Artificial Intelligence (AI) tools.

Acknowledgement

H. Kim was supported by Basic Science Research Program through the National Research Foundation of Korea (NRF) funded by the Ministry of Education (2021R1A6A1A03044326). Jyoti was supported by Brain Pool program funded by the Ministry of Science and ICT through the National Research Foundation of Korea (2022H1D3A2A02081237). The corresponding author (J.S. Kim) was supported by Korea University Grant. The authors express their gratitude to the reviewers for their valuable comments on this revised version.

References

[1] Y. Weng, W. Xu, Y. Wu, K. Zhou, B. Guo, 2D shape deformation using nonlinear least squares optimization, Vis. Comput. 22 (9) (2006) 653–660.
[2] W. Yang, Context-aware computer aided inbetweening, IEEE Trans. Vis. Comput. Graph. 24 (2) (2017) 1049–1062.
[3] S.Y. Lee, K.Y. Chwa, J. Hahn, S.Y. Shin, Image morphing using deformation techniques, J. Vis. Comput. Animat. 7 (1) (1996) 3–23.
[4] M. Steyvers, Morphing techniques for manipulating face images, Behav. Res. Methods Instrum. Comput. 31 (2) (1999) 359–369.
[5] H. Kim, C. Lee, S. Kwak, Y. Hwang, S. Kim, Y. Choi, J. Kim, Three-dimensional volume reconstruction from multi-slice data using a shape transformation, Comput. Math. Appl. 113 (2022) 52–58.
[6] R.W. Lewis, K. Ravindran, Finite element simulation of metal casting, Int. J. Numer. Methods Eng. 47 (2000) 29–59.
[7] H. Kim, S. Yoon, J. Wang, C. Lee, S. Kim, J. Park, J. Kim, Shape transformation using the modified Allen–Cahn equation, Appl. Math. Lett. 107 (2020) 106487.
[8] X. Qin, T. Wu, Y. Liu, A surface deformation method based on stiffness control, J. Adv. Mech. Des. Syst. Manuf. 14 (1) (2020) JAMDSM0010.
[9] L. Gao, J. Yang, Y.L. Qiao, P.L. Rosin, W. Xu, S. Xia, Automatic unpaired shape deformation transfer, ACM Trans. Graph. 37 (6) (2018) 1–15.
[10] S.M. Allen, J.W. Cahn, A microscopic theory for antiphase boundary motion and its application to antiphase domain coarsening, Acta Metall. 27 (6) (1979) 1085–1095.
[11] H. Kim, C. Lee, S. Yoon, Y. Choi, J. Kim, A fast shape transformation using a phase-field model, Extreme Mech. Lett. 52 (2022) 101633.
[12] Z. Han, H. Xu, J. Wang, A simple shape transformation method based on phase-field model, Comput. Math. Appl. 147 (2023) 121–129.
[13] H. Kim, S. Kang, G. Lee, S. Yoon, J. Kim, Shape transformation on curved surfaces using a phase-field model, Commun. Nonlinear Sci. Numer. Simul. 133 (2024) 107956.
[14] Y. Wang, X. Xiao, X. Feng, An efficient maximum bound principle preserving p-adaptive operator-splitting method for three-dimensional phase field shape transformation model, Comput. Math. Appl. 120 (2022) 78–91.
[15] Y. Wu, J. Yang, Z. Tan, A highly efficient variant of scalar auxiliary variable (SAV) approach for the phase-field fluid-surfactant model, Comput. Phys. Commun. 292 (2023) 108860.

[16] S. Biswas, D. Schwen, J. Singh, V. Tomar, A study of the evolution of microstructure and consolidation kinetics during sintering using a phase field modeling based approach, Extreme Mech. Lett. 7 (2016) 78–89.
[17] P.K. Amos, E. Schoof, J. Santoki, D. Schneider, B. Nestler, Limitations of preserving volume in Allen–Cahn framework for microstructural analysis, Comput. Mater. Sci. 173 (2020) 109388.
[18] H. Zhang, J. Yan, X. Qian, X. Chen, S. Song, Explicit third-order unconditionally structure-preserving schemes for conservative Allen–Cahn equations, J. Sci. Comput. 90 (2022) 1–29.
[19] B. Ji, H.L. Liao, Y. Gong, L. Zhang, Adaptive linear second-order energy stable schemes for time-fractional Allen–Cahn equation with volume constraint, Commun. Nonlinear Sci. Numer. Simul. 90 (2020) 105366.
[20] C. Liu, Z. Qiao, Q. Zhang, Two-phase segmentation for intensity inhomogeneous images by the Allen–Cahn local binary fitting model, SIAM J. Sci. Comput. 44 (1) (2022) B177–B196.
[21] Z. Qiao, Q. Zhang, Two-phase image segmentation by the Allen–Cahn equation and a nonlocal edge detection operator, arXiv preprint, arXiv:2104.08992, 2021.
[22] B. Xia, R. Yu, X. Song, X. Zhang, J. Kim, An efficient data assimilation algorithm using the Allen–Cahn equation, Eng. Anal. Bound. Elem. 155 (2023) 511–517.
[23] W. Xie, Q. Xia, Q. Yu, Y. Li, An effective phase field method for topology optimization without the curvature effects, Comput. Math. Appl. 146 (2023) 200–212.
[24] J. Wang, Z. Shi, Multi-reconstruction from points cloud by using a modified vector-valued Allen–Cahn equation, Mathematics 9 (12) (2021) 1326.
[25] H.G. Lee, J. Shin, J.Y. Lee, Energy quadratization Runge–Kutta scheme for the conservative Allen–Cahn equation with a nonlocal Lagrange multiplier, Appl. Math. Lett. 132 (2022) 108161.
[26] C. Cui, J. Liu, Y. Mo, S. Zhai, An effective operator splitting scheme for two-dimensional conservative nonlocal Allen–Cahn equation, Appl. Math. Lett. 130 (2022) 108016.
[27] Z. Sun, S. Zhang, A radial basis function approximation method for conservative Allen–Cahn equations on surfaces, Appl. Math. Lett. 143 (2023) 108634.
[28] Y. Li, S. Lan, X. Liu, B. Lu, L. Wang, An efficient volume repairing method by using a modified Allen–Cahn equation, Pattern Recognit. 107 (2020) 107478.
[29] J. Fieres, P. Schumann, C. Reinhart, Predicting failure in additively manufactured parts using X-ray computed tomography and simulation, Proc. Eng. 213 (2018) 69–78.
[30] L. Zhang, F. Belblidia, H.M. Davies, N.P. Lavery, S.G. Brown, D. Davies, Optimizing gate location to reduce metal wastage: Co-Cr-W alloy filling simulation, J. Mater. Process. Technol. 240 (2017) 249–254.
[31] H.M. Si, C. Cho, S.Y. Kwahk, A hybrid method for casting process simulation by combining FDM and FEM with an efficient data conversion algorithm, J. Mater. Process. Technol. 133 (2003) 311–321.
[32] L. Zhang, W. Tan, H. Hu, Determination of the heat transfer coefficient at the metal-sand mold interface of lost foam casting process, Heat Mass Transf. 52 (2016) 1131–1138.
[33] G.A. Hodbe, B.R. Shinde, Design and simulation of Lm 25 sand casting for defect minimization, Mater. Today Proc. 5 (2) (2018) 4489–4497.
[34] J. Yang, Y. Li, C. Lee, Y. Choi, J. Kim, Fast evolution numerical method for the Allen–Cahn equation, J. King Saud Univ., Sci. 35 (1) (2023) 102430.
[35] S. Ham, J. Kim, Stability analysis for a maximum principle preserving explicit scheme of the Allen–Cahn equation, Math. Comput. Simul. 207 (2023) 453–465.